Atomistic analysis of piezoelectric potential fluctuations in zinc-blende InGaN/GaN quantum wells: A Stillinger-Weber potential based analysis

Thomas P. Sheerin [1,2,*] Daniel S. P. Tanner,[3] and Stefan Schulz [1]

[1]*Tyndall National Institute, Lee Maltings, Dyke Parade, Cork T12 R5CP, Ireland*
[2]*Department of Physics, University College Cork, Cork T12 YN60, Ireland*
[3]*Laboratoire SPMS, CNRS-CentraleSupélec, Université Paris-Saclay, 91190 Gif-sur-Yvette, France*

In this paper we investigate strain and local polarization field effects in zinc-blende indium gallium nitride (InGaN) alloys and quantum wells. To do so we parametrize and establish a Stillinger-Weber potential with parameters fitted to hybrid functional density functional theory data. The developed model gives very good agreement with quantities to which it has not been fitted, such as Kleinman parameters of cubic III-N materials or the composition dependence of the lattice constant in InGaN alloys. Equipped with this model, we extract the composition dependence of elastic constants C_{11} and C_{12} in InGaN alloys, including bowing parameters for these quantities, which may form input for continuum-based calculations. Furthermore, applying this model to InGaN alloys and wells reveals that random alloy fluctuations can lead to strong local strain field fluctuations. Building on this information, we present a model that allows for the calculation of connected local built-in field fluctuations at the microscopic level, accounting for first- and second-order piezoelectric effects. The approach is general and can be applied to any zinc-blende III–V alloy or heterostructure investigated in the frame of semiempirical models (e.g., valence force field models) targeting strain fields on an atomistic level. Here, building on our Stillinger-Weber potential we show that local strain fluctuations in zinc-blende InGaN quantum wells can lead to strong piezoelectric built-in field fluctuations. This contribution has been widely overlooked in previous theoretical studies of these systems. Finally, we briefly discuss the impact of these polarization field fluctuations on carrier localization effects in such quantum well systems.

I. INTRODUCTION

In recent decades, the III-nitride semiconductors have emerged as among the most promising materials for many novel applications in areas, such as photovoltaics, microlight-emitting diodes (μ LEDs) and high-electron-mobility transistors [1–3]. In particular, indium gallium nitride (InGaN)/GaN heterostructures grown along the c axis of the wurtzite (WZ) crystal phase form the basis for modern high-efficiency blue LEDs which have revolutionized the field of solid-state lighting [4–7]. In principle, the emission wavelength of InGaN alloys can be tailored to span across the entire visible spectrum by varying the InN content; however, WZ InGaN-based LEDs suffer an efficiency drop in the green spectral range and at longer wavelengths [8–11]. Since there are currently no other materials that emit efficiently in the green spectral range, this gives rise to the so-called "green gap" problem.

This efficiency drop is, in part, attributable to the presence of very strong electrostatic built-in fields arising from strain-independent ("spontaneous") and strain-dependent ("piezoelectric") polarization fields in c-plane WZ InGaN quantum wells (QWs). These fields localize electrons and holes to opposite interfaces of the well thereby lowering the

wave-function overlap and, consequently, the radiative recombination probabilities [10,12–16]. A number of potential ways to reduce these electrostatic built-in fields, originating from both the underlying WZ structure and the growth along the c axis, have been considered by previous studies. Previously, growth of heterostructures along semi-/nonpolar directions in the WZ crystal structure [17–24], growth of ultrathin InGaN layers [25,26], as well as the use of the metastable zinc-blende (ZB) phase [27–30] have been considered.

In this paper, we focus on the last of these approaches since it has several distinct potential benefits when compared to WZ-based systems. First, ZB InN and GaN have slightly smaller band gaps than their WZ counterparts [31,32] so that less InN content is required in order to reach the green/yellow spectral region. This is an advantage as incorporation of large amounts of In is experimentally challenging [33]. Second, in an ideal picture, QW structures utilizing the ZB (cubic) phase of the constituent nitride materials and grown along the [001] direction of the crystal should present no *macroscopic* spontaneous [34] or piezoelectric-related built-in fields, given the absence of shear strain [35,36]. Thus, ZB InGaN wells offer a promising route to closing the green gap.

However, it is important to note that alloy fluctuations and, thus, the associated strain field fluctuations in (for instance) an InGaN alloy may lead to *local* built-in fields which fluctuate on small length scales. It has been shown in the literature that these potential fluctuations are present in WZ InGaN

---
[*]116352193@umail.ucc.ie

systems and have both beneficial and detrimental effects on radiative recombination rates in this alloy [12,37]. On the one hand, it has been demonstrated in the literature that alloy fluctuations and, thus, the connected potential fluctuations in *c*-plane WZ InGaN QWs give rise to strong carrier localization effects [10,37–41]. These localization effects are widely assumed to explain [12,13] the insensitivity of the efficiency of InGaN-based devices emitting in the violet-blue spectral region to the very high defect densities present in these structures (these can be $\sim 10^9$ cm^{-2} [6]). On the other hand, such carrier localization effects can cause in-plane separation of holes and electrons in these QWs [10,38,42], which further reduces the wave-function overlap and is, thus, deleterious for the efficiency of the device. Furthermore, theoretical studies of *bulk* ZB InGaN have shown that atomistic effects are also likely to play a prominent role in this material [43–45]. On the whole, random alloy effects must be taken into account to achieve an accurate description of the electronic and optical properties of these systems. However, although some previous atomistic calculations have been performed on *bulk* ZB InGaN [43–47], all works [28,30,48,49] that have theoretically studied ZB InGaN QWs employed continuum models which, by their nature, neglect atomistic effects and, thus, alloy-induced polarization fields. These studies also neglected the deviation from linear variation of the elastic constants, which has been shown to impact transition energies in wurtzite systems by up to 25 meV [50].

We also stress that local alloy-induced effects in III-N materials, such as InGaN, are expected to be much more pronounced when compared to other III–V ZB materials, e.g., InGaAs. This stems, for instance, from the fact that the piezoelectric coefficients in InN and GaN are at least a factor of order two larger than those of InAs or GaAs [51]. Furthermore, whereas the lattice mismatch between InAs and GaAs is $\approx 7\%$, this mismatch is $\approx 10\%$ [51] in the case of GaN and InN. All these factors will amplify the impact of alloy fluctuations on the local built-in fields, and findings on InGaAs systems cannot necessarily be carried over to an InGaN alloy.

In this paper, we take a first step towards filling this gap by performing an atomistic analysis of strain effects and the local built-in piezoelectric potential in an InGaN/GaN QW. Given that highly accurate *ab initio* approaches, such as "standard" density functional theory (DFT) are too computationally heavy to simulate nanoscale objects, such as heterostructures where supercells with several thousands of ions must be considered, we present, develop, and use a semiempirical interatomic potential to achieve this goal. For reasons outlined in Sec. II, we choose the Stillinger-Weber (SW) interatomic potential. Our theoretical framework, thus, allows the relaxed atomic positions to be found so that Poisson's equation may subsequently be solved to obtain the electrostatic potential arising from the resulting local strain field. The presented approach includes first- and second-order piezoelectric effects and can be applied to other ZB material systems for which strain effects are to be targeted in a microscopic picture. Overall, our framework, therefore, gives an ideal starting point for future atomistic electronic structure calculations, employing, for instance, semiempirical tight-binding models [52].

The results of our analysis of the binary III-nitrides and bulk InGaN show that the SW potential makes predictions for these materials that are quantitatively similar to those from highly accurate hybrid functional DFT, indicating that the potential is suitable for such purposes. Building on these findings, we extract bowing parameters for the evolution of elastic constants with InN content; this information can be used in continuum-based calculations where evolution of the material parameters with alloy content is required. Furthermore, we provide insight into the magnitude and impact of local strain effects by studying the distributions of bond lengths and two-body interaction energies extracted from various InGaN supercells. Finally, our analysis of an In$_{0.15}$Ga$_{0.85}$N/GaN QW reveals large local fluctuations in the strain and piezoelectric potential, an aspect widely ignored in the literature. Overall, the scale of these fluctuations supports strong (hole) wave-function localization in ZB III-nitride QWs, an effect which is likely to have a large impact on the properties of devices based on these wells.

The paper is organized as follows. In Sec. II, we outline the theoretical basis of the paper. Then, in Sec. III A, we investigate and benchmark the developed SW model by extracting quantities, namely, the Kleinman parameters to which the model has not been fitted and comparing them to hybrid functional DFT data from the literature. In Sec. III B we focus on bulk properties of ZB InGaN alloys predicted by the potential, whereas in Sec. III C a ZB InGaN/GaN QW is targeted, including an analysis of the piezoelectric potential arising from first- and second-order effects. Finally, we summarize our work in Sec. IV.

II. THEORETICAL FRAMEWORK

In this section, we describe the theoretical models used in the paper. In Sec. II A, the SW potential is introduced, and the parameter-fitting procedure delineated, whereas in Sec. II B, the method utilized to calculate the local built-in piezoelectric potential in a QW is described in detail.

A. Stillinger-Weber potential

We seek an accurate description of microscopic atomistic effects while retaining the ability to model systems containing thousands of atoms. Semiempirical interatomic potentials, being classical approximations to the interactions between ions, are well suited to these requirements as they explicitly take account of each ion in the system but are much faster than *ab initio* approaches. Numerous different models have been used in the past [53–59]. In this paper, we use the SW potential, implemented using the software package GULP [60,61]. This potential is among the simplest and, hence, is ideal for large-scale simulations but is also particularly well suited to describing directional bonds in tetrahedrally bonded crystals. Valence force field models can also do this, but Coulombic effects must be included to accurately describe the III-nitrides due to their high bond ionicity [55], and inaccuracies may persist even with this adjustment [62].
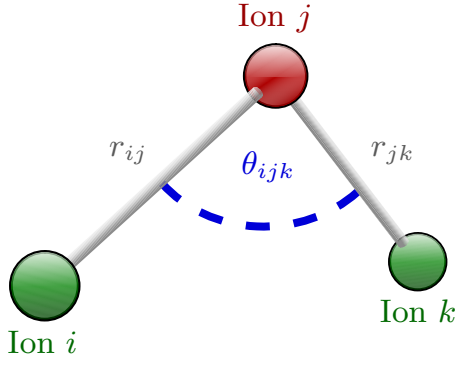
FIG. 1. Schematic of a triplet of ions in the lattice with bond lengths and angles from Eq. (4) marked.

Stillinger and Weber [57] approximated the potential energy of the unit cell as a sum of two- and three-body terms,

$$U(\mathbf{r}_1, \mathbf{r}_2, \ldots, \mathbf{r}_n) = \sum_{\substack{i, j \\ i < j}} v_2(r_{ij}) + \sum_{\substack{i, j, k \\ i < j < k}} v_3(\mathbf{r}_i, \mathbf{r}_j, \mathbf{r}_k), \quad (1)$$

where the $\mathbf{r}_i$'s are the positions of the n ions in the unit cell and $i, j, k = 1, \ldots, n$ are subject to the inequalities, which ensure each pair or triple is counted exactly once. r_{ij} is the distance between ions i and j. The function v_2 has the profile of a typical two-body interaction and is written as the product of a rational function (which goes to infinity at zero) and an exponential that brings the potential to zero at the cutoff distance a_{ij} with continuity of all derivatives,

$$v_2(r_{ij}) = \begin{cases} A_{ij}(B_{ij}r_{ij}^{-4} - 1) \exp\left(\frac{\sigma_{ij}}{r_{ij} - a_{ij}}\right), & \text{if } r_{ij} < a_{ij}, \\ 0, & \text{if } r_{ij} \geqslant a_{ij}. \end{cases} \quad (2)$$

One always assumes that the parameters A_{ij}, B_{ij}, σ_{ij}, and a_{ij} for any two ions depend only on their species. In the following we consider an ideal lattice (e.g., no defects), thus, a given cation will only get close enough to interact with its neighboring anions and vice versa (e.g., Ga ions in GaN usually only have N ions as nearest neighbors); so each binary material requires only one such parameter set, namely, $\{A, B, a, \sigma\}$.

The three-body contribution from each distinct triplet of ions (see Fig. 1 for a schematic) is written as [57]

$$v_3(\mathbf{r}_i, \mathbf{r}_j, \mathbf{r}_k) = h(r_{ij}, r_{jk}, \theta_{ijk}) + h(r_{ik}, r_{ij}, \theta_{kij}) \\ + h(r_{jk}, r_{ik}, \theta_{jki}), \quad (3)$$

where θ_{ijk} is the angle subtended at ion j, etc. The term $h(r_{ij}, r_{jk}, \theta_{ijk})$ is nonzero only if $r_{ij} < a_{ij}$ and $r_{jk} < a_{jk}$ whereupon,

$h(r_{ij}, r_{jk}, \theta_{ijk})$

$$= \lambda_{ijk} \exp\left(\frac{\gamma_{ij}}{r_{ij} - a_{ij}} + \frac{\gamma_{jk}}{r_{jk} - a_{jk}}\right)(\cos\theta_{ijk} - \cos\theta_0)^2, \quad (4)$$

and similarly for the other two terms. We set $\theta_0 = \arccos(-1/3)$, the ideal tetrahedral angle in ZB so that v_3 explicitly includes strong directional bonding. As above, in this paper only cation-nitrogen nearest-neighbor distances become less than the cutoff distances, so $h(r_{ij}, r_{jk}, \theta_{ijk})$ is nonzero only if there is a cation where θ_{ijk} is subtended and nitrogen

ions at the other two sites or vice versa. Hence, a binary material has only four free three-body parameters: λ_N, γ_N, λ_C, and γ_C where the subscript denotes the species that lies where θ_{ijk} is subtended (N: nitrogen; C: cations, e.g., Ga, In or Al). Correspondingly, at most one of the terms in Eq. (3) will be nonzero as at least one of r_{ij}, r_{ik}, and r_{jk} will be greater than the cutoff distance. Note that in the above, most parameters are defined so that they differ from the original definitions of Stillinger and Weber [57] by a factor containing σ or ε (the energy unit), e.g., $A = \varepsilon A_{SW}$, $B = \sigma^4 B_{SW}$, etc.

To determine values for the different parameters, we treat them as free and adjustable, thereby enabling the SW model to reproduce key material properties, such as elastic constants. We note here that the primary focus of our paper consists of the binary materials InN, GaN, and the corresponding alloy InGaN. However, in the model development we also target AlN so that the potential may also be used to study, for instance, AlGaN-based heterostructures. Thus, we derive SW parameters for all three cubic binary materials. Here, we opt to fit the parameters such that the SW potential reproduces two of the three independent elastic constants of the ZB binary materials, namely, C_{11} and C_{12} (in Voigt notation) and the cohesive energy per bond ($-\varepsilon$). In addition, although we do not include it explicitly in the least-squares fitting procedure, if the lattice parameter a_0 of a given parameter set deviates significantly from literature values, the set is discarded. As few reliable experimental data for the full elastic tensor of the cubic nitrides exist, we use data obtained by Caro *et al.* [63] using hybrid-functional DFT (HSE06) as a reference point for our paper. Their lattice parameters are also used (which differ by $< 1\%$ from experimentally determined values [31,32,64]) as reference values for data predicted from our SW potential. A number of studies have estimated the bond energies of the III-nitrides, and we take the averages of those given in Refs. [65–69]; the averages are of the order of eV and the standard deviations are all $\lesssim 0.07$ eV. The values fitted to (as well as the values of C_{44} and a_0) are presented in Table I along with those predicted by our SW potential and the deviations.

The fitting of the model to material parameters utilizes GULP's built-in capabilities; GULP fits to observables α_i^{fit} by minimizing the sum of squares function $S = \sum_{i=1}^{N_{\text{obs}}} w_i(\alpha_i^{\text{fit}} - \alpha_i)^2$ using the Newton method with a Broyden-Fletcher-Goldfarb-Shanno update of the Hessian at each iteration [60,61]. Any choice may be made for each of the weighting factors w_i—however, we find that a good fit cannot be made to all three elastic constants (regardless of whether or not we fit to ε).

In this paper, we are mainly concerned with modeling QWs grown along the [001] direction of the ZB crystal. In a continuum-based model, as we will discuss in more detail below, the strain along the growth direction is mainly determined by the ratio C_{11}/C_{12}. Thus, we aim to describe this contribution accurately. Other semiempirical models targeting strain fields in ZB heterostructures follow the same procedure and mainly target the elastic constants C_{11} and C_{12} in their parametrization (e.g., Keating-like potentials used in the description of the strain field in [001]-grown heterostructures, such as quantum dots [54,55,70,71]). Indeed, in Ref. [72] the author shows that a parametrization of the Keating model

TABLE I. Material parameters for InN, GaN, and AlN. The literature elastic constants and lattice parameters are taken from Ref. [63], whereas the bond energies are averages of those from Refs. [65,66,68] (for InN), Refs. [65,67] (for GaN), and Refs. [65,67–69] (for AlN). The literature and predicted (by our potential) material parameters are denoted by the superscripts "lit" and "pred," respectively. The table also gives the error in the different quantities (in percentages). More details are given in the main text.

	InN	GaN	AlN
$\varepsilon^{\mathrm{pred}}$ (eV)	2.001	2.232	2.829
$\varepsilon^{\mathrm{lit}}$ (eV)	2.001	2.233	2.829
Error (%)	0.000	−0.045	0.000
C_{11}^{pred} (GPa)	183.200	288.600	308.900
C_{11}^{lit} (GPa)	183.200	288.600	308.900
Error (%)	0.000	0.000	0.000
C_{12}^{pred} (GPa)	119.200	154.100	166.500
C_{12}^{lit} (GPa)	119.200	154.100	166.500
Error (%)	0.000	0.000	0.000
C_{44}^{pred} (GPa)	53.227	103.422	109.895
C_{44}^{lit} (GPa)	91.500	166.000	196.000
Error (%)	−41.828	−37.698	−43.931
a_0^{pred} (Å)	4.988	4.489	4.363
a_0^{lit} (Å)	4.988	4.489	4.363
Error (%)	0.000	0.000	0.000

which gives more importance to C_{44} over C_{11} and C_{12} is unsuited to describing ZB systems grown along [001]. Thus, we weight C_{11}, C_{12}, and ε equally and do not include C_{44} in GULP's least-squares minimization routine. With this approach we find a perfect fit to the first three (see Table I). Also, and even though not fitted to, perfect agreement with the DFT lattice constants is found. As can be seen from Table I, the deviations of the predicted values from the targets are larger in the case of C_{44}. However, we note that, for instance, the widely applied Keating model exhibits deviations in C_{44} values of similar magnitude, and as explained above, these deviations are expected to be of secondary importance for the systems under consideration in this paper.

The optimal parameters for our SW model are presented in Table II. We briefly note that, with the exception of A, they are monotonic or constant in the atomic number of the

TABLE II. The SW parameter sets obtained for all three cubic binary nitrides. The subscripts N and C refer to nitrogen and cation (Ga, In, and Al) related parameters, respectively. They are discussed in the text.

Parameter	InN	GaN	AlN
A (eV)	15.661	15.950	10.996
B (Å^4)	8.807	5.574	4.220
a (Å)	3.382	3.060	2.800
σ (Å)	1.881	1.642	0.870
γ_{C} (Å)	2.196	1.767	1.445
γ_{N} (Å)	2.196	1.767	1.465
λ_{C} (eV)	31.661	31.661	31.661
λ_{N} (eV)	31.661	31.661	31.661

cation species. The decrease in A as we move from GaN to AlN is somewhat of an anomaly as A is proportional to ε when all other parameters are fixed, and ε is largest for AlN. However, when all parameters vary (as they do here), changes in the others compensate for the behavior of A for AlN. Also, as stated previously, AlN plays no further role in this paper. Note too that the three-body constants in a given material are almost exactly equal for the cases of N-centered interactions (i.e., with a N ion where the angle is subtended and C ions on the other two sites) and C-centered interactions, e.g., $\gamma_{\mathrm{N,InN}} = \gamma_{\mathrm{C,InN}}$. That is, the N-centered and C-centered three-body interactions are identical in a given binary. This is perhaps not entirely surprising, and many previous studies using the SW potential have enforced this equality during fitting [67,73,74]. We also see that the λ constants are the same across all three materials by construction—we decided to fit $\lambda_{\mathrm{C,InN}}$ and $\lambda_{\mathrm{N,InN}}$ as free parameters and then fix the λ constants for GaN and AlN to these values. Such an approach is advantageous for simulation of ternary alloys since no averaging protocol is then required when determining the three-body constants for a mixed triplet of ions (e.g., with one N, one Ga, and one In). We chose the constants of InN as the reference because correctly describing strain around In sites in low-x In$_x$Ga$_{1-x}$N is likely to be crucial for modeling of InGaN/GaN heterostructures.

B. Theory of local polarization

As already discussed above, due to their cubic symmetry, ZB materials do not exhibit a spontaneous polarization [34] and when grown along the [001] direction, pure ZB QWs (no alloy fluctuations and biaxial strain only) are free from piezoelectric fields. This ideally grants a distinct advantage over WZ c-plane systems in the exploitation of heterostructures for optoelectronic device applications. However, in the presence of *local* shear strain, a *local* piezoelectric polarization field $\mathbf{P}(\mathbf{r})$ may be induced. Compared to other ZB III–V materials, local effects should be much larger in ZB III-N alloys given their (in general) much larger piezoelectric coefficients [51]. Also, it has been shown [41,75] that in polar and nonpolar WZ systems such fields fluctuate significantly on the scale of a few angstroms and are of much importance in accurately describing the electronic and optical properties of WZ InGaN-based heterostructures [39,41]. However, in ZB III-N alloys and heterostructures, this effect has not been studied so far. We present in the following a framework which allows us to gain insight into these questions and is a general approach that can also be applied to other ZB heterostructures.

A number of previous works [35,36,76–78] have demonstrated the significance of second-order piezoelectric effects in ZB III–V materials, and $\mathbf{P}(\mathbf{r})$ can be written as a sum of terms first- and second-order in strain [36],

$$\mathbf{P}(\mathbf{r}) = e_{14} \begin{pmatrix} \epsilon_4 \\ \epsilon_5 \\ \epsilon_6 \end{pmatrix} + B_{114} \begin{pmatrix} \epsilon_1\epsilon_4 \\ \epsilon_2\epsilon_5 \\ \epsilon_3\epsilon_6 \end{pmatrix} + B_{124} \begin{pmatrix} (\epsilon_2 + \epsilon_3)\epsilon_4 \\ (\epsilon_1 + \epsilon_3)\epsilon_5 \\ (\epsilon_1 + \epsilon_2)\epsilon_6 \end{pmatrix}$$
$$+ B_{156} \begin{pmatrix} \epsilon_5\epsilon_6 \\ \epsilon_4\epsilon_6 \\ \epsilon_4\epsilon_5 \end{pmatrix}, \quad (5)$$

where the ϵ_i's are the strain tensor components, e_{14} is the single independent component of the first-order piezoelectric tensor, and B_{114}, B_{124}, and B_{156} are those of the second-order tensor (all in Voigt notation). This polarization, in turn, gives rise to a charge-density ρ, with

$$\rho(\mathbf{r}) = -\nabla \cdot \mathbf{P}(\mathbf{r}). \qquad (6)$$

Knowledge of $\rho(\mathbf{r})$ then allows Poisson's equation to be solved for the associated built-in electrostatic potential $\phi(\mathbf{r})$,

$$\nabla^2 \phi(\mathbf{r}) = -\frac{\rho(\mathbf{r})}{\varepsilon^D}. \qquad (7)$$

Here we use a constant and position-independent static electric permittivity ε^D. Given that the built-in field in the present case mainly arises from local strain fluctuations within the well, we set $\varepsilon^D = \varepsilon^D_{\text{InGaN}}$, obtaining $\varepsilon^D_{\text{InGaN}}$ from a linear interpolation of the dielectric constants from GaN and InN. Furthermore, given that in the following we are interested in relatively low InN contents of 15%, the dielectric mismatch will be small. Taking all this together, and for a first insight into the impact of local alloy fluctuations on local built-in potential fluctuations, assuming a constant and position-independent ε^D should be sufficient for our purposes. To implement the above procedure, we follow the approach used in Refs. [79,80]. The strain tensor is first defined at each ionic site by the deviation of the four nearest neighbors from ideal positions. As an example, we consider a N ion and its four nearest-neighbor cations C_i. Each cation is assigned an unstrained position $\mathbf{r}_i^0$ relative to the N ion based on the ideal tetrahedral angle and the equilibrium bond length of C_iN—e.g., given two In and two Ga nearest neighbors, the nominal positions might be

$$\mathbf{r}_1^0, \mathbf{r}_2^0 = a_0^{\text{InN}}\left(\pm\tfrac{1}{4}, \pm\tfrac{1}{4}, \tfrac{1}{4}\right),$$
$$\mathbf{r}_3^0, \mathbf{r}_4^0 = a_0^{\text{GaN}}\left(\pm\tfrac{1}{4}, \mp\tfrac{1}{4}, -\tfrac{1}{4}\right).$$

After ionic relaxation, the four relative positions are denoted by $\mathbf{r}_i$. We form three linearly independent vectors to span the nearest-neighbor tetrahedron as follows:

$$\mathbf{R}_1 = \mathbf{r}_2 - \mathbf{r}_1,$$
$$\mathbf{R}_2 = \mathbf{r}_4 - \mathbf{r}_3,$$
$$\mathbf{R}_3 = \tfrac{1}{2}(\mathbf{r}_4 + \mathbf{r}_3 - \mathbf{r}_2 - \mathbf{r}_1),$$

and similarly before relaxation. The strained vectors are then obtained from the unstrained by a matrix M so that $\mathbf{R}_j = M\mathbf{R}_j^0$ for $j = 1$–3. Because the "local tetrahedron basis" may rotate slightly during relaxation, we must perform a polar decomposition to extract the symmetric matrix ϵ,

$$M = (\mathbb{1} + \epsilon)O, \qquad (8)$$

where O is an orthogonal matrix. Given ϵ, $\mathbf{P}$ is evaluated using piezoelectric coefficients from Ref. [51] such that we approximate the coefficients at a cation C by those for CN and at a N site we average over nearest neighbors.

All derivatives in Eqs. (6) and (7) are next approximated by finite differences, evaluated on the irregular grid formed by the relaxed ionic positions [80]. This allows direct computation of the divergence in Eq. (6), whereas in Eq. (7) it reduces to a system of n linear equations in the values of ϕ at the positions
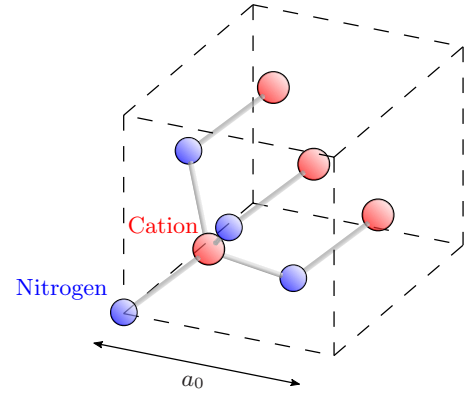

FIG. 2. The (nonprimitive) ZB unit cell used in this paper. The colors blue/red denote the two sublattices.

of the n ions in the system (details of the calculation of ϕ are given in the Appendix).

III. RESULTS

The following summarizes the results obtained in this paper. In Sec. III A we test the capability of our SW model by using it to predict the Kleinman/internal strain parameter [81] for each of the binary III-nitrides since this parameter is tightly linked to the piezoelectric response of a material. Then, in Sec. III B we present some of the predictions made by the potential for bulk InGaN. Finally, Sec. III C details the results of our investigation of the local polarization field in an InGaN/GaN QW with 15% InN content in the well layer.

A. Prediction of the Kleinman parameter

A good test of the accuracy of an interatomic potential is its ability to predict material properties to which it is not explicitly fitted. Since we are interested in local piezoelectric effects, we choose the Kleinman parameter (internal strain parameter) ζ as such a benchmark; ζ is tightly linked to the ionic part of the first-order piezoelectric coefficient [51].

When a lattice is held under a uniform strain, the ions in each unit cell may relax internally to a lower-energy state, that is, the sublattices may shift relative to each other. In the ZB structure, there are two sublattices so that one will be moved relative to the other under the direct influence of the strain plus any potential internal displacement. For example, in Fig. 2, using coordinates in which the labeled nitrogen ion is fixed, the position $\mathbf{r}$ of the cation after strain is given by

$$\mathbf{r} = (\mathbb{1} + \epsilon)\mathbf{r}_0 + \mathbf{t}, \qquad (9)$$

where $\mathbf{r}_0$ is its initial position, ϵ is the strain tensor, and $\mathbf{t}$ is the (single) internal displacement vector for the ZB lattice [54,63]. Using Cartesian coordinates aligned along the principal directions of the unit cell we have, to first order in strain [54,63],

$$\mathbf{t} = -\frac{a_0 \zeta}{2}(\epsilon_{yz}, \epsilon_{xz}, \epsilon_{xy}), \qquad (10)$$

where a_0 is the equilibrium lattice constant and ζ is the Kleinman/internal strain parameter (dimensionless). We restrict our
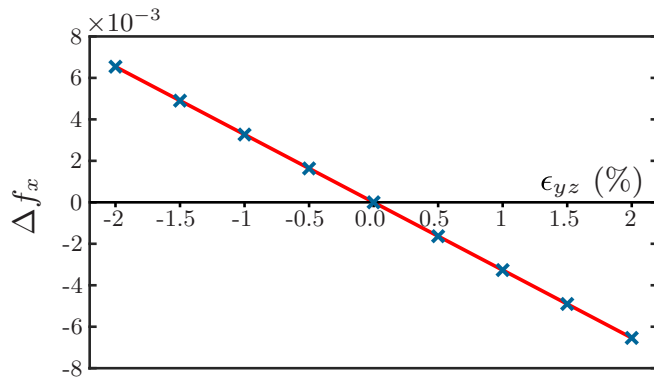
FIG. 3. Change in the fractional x coordinate of cation vs external strain for GaN. The crosses are numerical data points whereas the line is a linear fit.
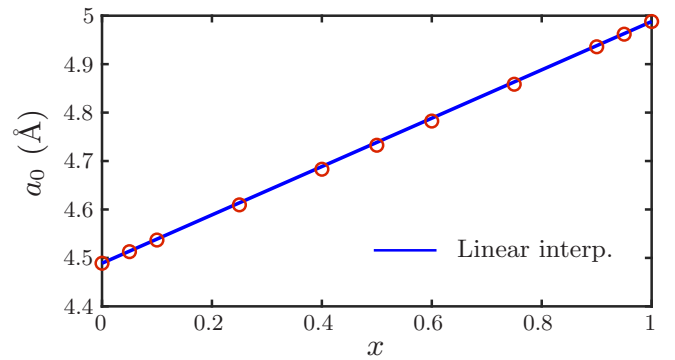

FIG. 4. The lattice constants of a number of $In_xGa_{1-x}N$ supercells, plotted against x. The linear interpolation is the heuristic expectation from Vegard's law.

analysis to contributions to first-order in strain; higher-order terms [51] which may come into play are beyond the scope of the present paper.

Applying a strain with all zero components except ϵ_{yz} [i.e., $\epsilon = (0, 0, 0, 2\epsilon_{yz}, 0, 0)$ in Voigt notation], and if the final and initial fractional coordinates of the cation are (f_x, f_y, f_z) and (f_{x0}, f_{y0}, f_{z0}), respectively, then,

$$f_x - f_{x0} = \Delta f_x = -\frac{\zeta}{2}\epsilon_{yz}. \tag{11}$$

The variation, predicted by the SW potential, of Δf_x with ϵ_{yz} is then fitted with a linear function from which ζ is found. All calculations have been performed over a strain range of $-2\% \leqslant \epsilon_{yz} \leqslant 2\%$, which is small enough so that a first-order internal-strain approximation should still be valid but large enough to avoid numerical noise. Figure 3 shows as an example the results obtained for GaN. The linear fit is clearly very good, and the same is true for InN and AlN (with a correlation coefficient greater than 0.999 in all three cases), confirming that the strain range is indeed small/large enough.

The values of ζ found are given in Table III where we have also included hybrid DFT values from Ref. [63] for comparison since there are no experimental data on this parameter for the cubic III-nitrides. In the case of InN, the agreement with the *ab initio* value is remarkable, whereas for GaN there is some deviation, but the match is reasonably good, and for AlN the deviation is more pronounced. However, in the following we focus our attention on InGaN-based systems. Therefore, the level of agreement with the DFT literature results is very satisfactory for our purposes and further confirms the suitability of the developed model.

TABLE III. The values of the Kleinman parameter ζ predicted by the SW potential and the data obtained by Caro *et al.* [63] (ζ^{DFT}) using hybrid functional DFT data. The percentage deviations between the SW and the DFT values are also given.

	InN	GaN	AlN
ζ	0.748	0.654	0.658
ζ^{DFT}	0.760	0.580	0.545
Error (%)	−1.579	12.759	20.734

B. Bulk InGaN

Here, we study bulk $In_xGa_{1-x}N$ systems with various values of InN content x. In the following we assume that InGaN is a random alloy, here carrying information over from InGaN wurtzite systems [75]. In our numerical framework this is accomplished by constructing and relaxing supercells which contain In and Ga ions placed at cation sites according to a simple random number generator with their total numbers being in the ratio x:$1 - x$. In doing so we have access, where needed, to the impact of the alloy microstructure on the results. For the InN contents $x = 0.25$, $x = 0.5$, and $x = 0.75$ we have generated three different microscopic alloy configurations each. Our investigations revealed (see the discussion below) that for each of these InN contents the calculated properties varied only slightly with alloy configuration. Thus, for $x = 0.1$, $x = 0.4$, $x = 0.6$, and $x = 0.9$ we have evaluated the material properties for one random alloy configuration. In deciding on optimal supercell size, one must balance computation time against the need to make the cell as large as possible in order to best mimic a truly random structure. We have opted for a cell consisting of $11 \times 11 \times 11$ unit cells of the ZB structure (a unit cell, containing eight atoms, is depicted in Fig. 2), so that 10 648 atoms are included in the simulation. Such system sizes are beyond the capabilities of standard DFT. Having the same initial dimensions along each of the Cartesian directions ensures that any artificial effects introduced by the periodic boundary conditions apply roughly isotropically.

We first study the evolution of the lattice constant with x. After relaxation, we take the lattice constant a_0 as $\frac{1}{11} \times$ the average of the lengths of the three final lattice vectors. Because these lengths show such little variation at a given x, differing from each other by no more than 0.01 Å, we only relax one random configuration per value of x. The lattice constant a_0 is shown as a function of the InN content x in Fig. 4. The lattice constant a_0 displays an almost perfectly linear variation with x; a linear interpolation between the end points is shown in the figure with the fit only improving very slightly when we adopt a quadratic model. This linear variation of the lattice constant with alloy content x is in excellent agreement with experimental [33] and DFT [47,82] data. This further supports and strengthens that the developed SW model

provides accurate insight into strain effects in InGaN alloys, even though the model is parametrized by using binaries only.

In a second step, we use the potential to extract further properties of bulk ZB InGaN. One feature of $In_xGa_{1-x}N$ that is of much interest is the dependence of its elastic constants on x. This information is particularly useful as input to continuum-model simulations of large structures, such as InGaN-based diodes, wherein the large strains between adjacent material layers must be modeled accurately. GULP features built-in functions that calculate the elastic constants of a supercell from second derivatives of the energy density. We implement this functionality to find C_{11}, C_{12}, and C_{44} for $In_xGa_{1-x}N$ at a number of values of x and then apply quadratic fits to derive the bowing parameters. The results presented below for $x = 0.25$, $x = 0.5$, and $x = 0.75$ are obtained from an average over the three considered alloy configurations. We have observed that the spread in the calculated data is very small so that for $x = 0.1$, $x = 0.4$, $x = 0.6$, and $x = 0.9$ only one alloy configuration is used to obtain the elastic constants. If one excludes the data points evaluated at $x = 0.1$, $x = 0.4$, $x = 0.6$, and $x = 0.9$ (one alloy configuration) in the fitting procedure described below, the extracted bowing parameters deviate by less than 1%. This indicates that employing one alloy configuration is a reasonable approximation here. The fits are always forced through the respective binary end points, i.e., the only degree of freedom in each fit is the bowing parameter b_{ij} (for $ij = 11$, 12, or 44). That is, the fit is of the form

$$C_{ij}(x) = (1-x)C_{ij}^{GaN} + xC_{ij}^{InN} - b_{ij}x(1-x).$$

Since the SW potential is fitted to DFT elastic constants C_{11} and C_{12} of the binaries, and since the potential has been shown to predict structural properties, such as the lattice constant evolution with InN content of the ternary material reliably, it can be expected that the SW potential also gives a good description of the composition dependence of C_{11} and C_{12} in InGaN. The bowing parameters we derive are $b_{11} = 35.64$ GPa and $b_{12} = 0.68$ GPa for C_{11} and C_{12}, respectively; the value of b_{11} we predict is over twice that found in Ref. [83], although our value for b_{12} is very similar to their figure of 1.00 GPa (a Keating potential was used in that work). A graphical representation of $C_{11}(x)$ and $C_{12}(x)$ is shown in Fig. 5. On the other hand, as explained in Sec. II, the values of C_{44} predicted by the SW potential for the binaries differ by ~40% from the literature, so we do not display the x dependence of C_{44} in Fig. 5. However, as all the C_{44} values suffer similar errors, the bowing parameter may be roughly unaffected. For the sake of completeness, the bowing parameter found for C_{44} amounts to $b_{44} = 23.41$ GPa.

Next, we study the effects of local alloy fluctuations on the local strain relaxation. In a binary material, all bond lengths are the same, and plotting these on a frequency histogram yields a single nonempty bin centered around the equilibrium bond length. Introducing quantities of another material should result in the appearance of two peaks near the equilibrium bond lengths of the binary constituents with each peak widened due to local distortion. Such bond length distributions are displayed in Fig. 6 for two of the studied supercells, one with 50% InN and the other with 10% InN. The equilibrium bond lengths of GaN and InN (b_0^{GaN} and
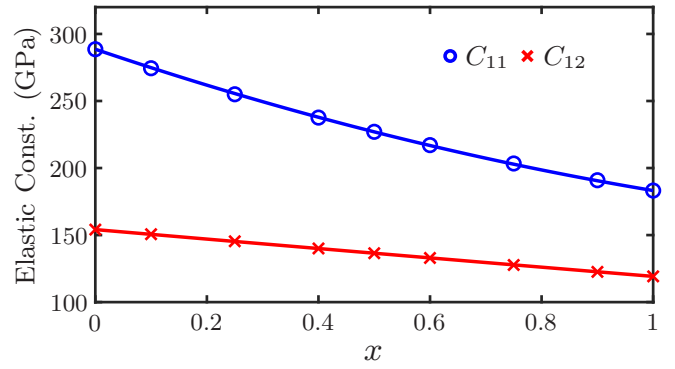

FIG. 5. Elastic constants C_{11} and C_{12} of zinc-blende $In_xGa_{1-x}N$ alloys as a function of the InN content x. The solid lines represent quadratic fits to the data. More details are given in the main text.

b_0^{InN}, respectively) are illustrated by dashed vertical lines, and each distribution is scaled so that the height of each bin gives its probability (i.e., frequency/21 296, where 21 296 is the number of bonds in a supercell). In the 50% case, the two peaks bound roughly equal areas, corresponding to one-half In-N bonds and the other half Ga-N. Each peak can be seen to be displaced towards the other, away from the ideal bond lengths, indicated by the vertical lines. Thus, as expected, the presence of cation C_1 in the alloy tends to perturb the C_2-N bonds towards the bond length of C_1N and vice versa.

In fact, the degree to which the peaks are displaced from the ideal may be taken as an approximate measure of the severity of local strain effects in the system. In a given distribution, we may consider each peak individually (as they are separated by a large gap containing no counts) and take the average of all bond lengths associated with the peak in question. The fractional deviation of this average from the associated equilibrium bond length then gives a rough measure of the local strain corresponding to that peak. For example, the mean bond length in the "GaN peak" in the $x = 0.5$ distribution is 1.970 Å, which differs by +1.345% from b_0^{GaN}—this percentage is an approximation to the typical local strain about a Ga-N bond in the material. Note that the + sign denotes tensile strain, whereas negative strains are compressive. The
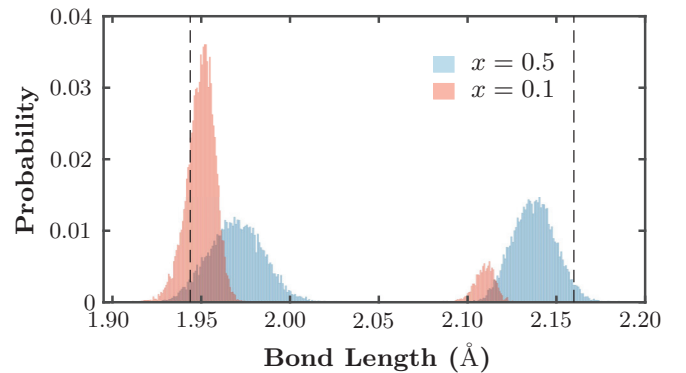

FIG. 6. Bond length distributions for InGaN supercells at 50% ($x = 0.5$) and 10% ($x = 0.1$) InN. The cells are not strained to a substrate (see below), and the vertical lines indicate the bond lengths of GaN (left) and InN (right).

strain associated with the "InN peak" in this distribution is about the same in magnitude at -1.047% but opposite in sign—that is, the In-N bonds are usually compressed as would be expected since InN has a larger bond length than GaN. Then, in the $x = 0.1$ distribution the GaN and InN peaks correspond to respective strains of 0.323% and -2.339%. The evolution of the distribution is, thus, clear: As x approaches 0, the InN peak becomes smaller, and both peaks move towards b_0^{GaN} as the increasing number of Ga ions has a stronger influence on the In-N bonds. The Ga-N bonds experience, on average, almost no strain in the dilute ternary, whereas the In-N bonds suffer large compressive (negative) strains. This is qualitatively in line with the expected trend, but the $\sim -2\%$ average local strain gives new quantitative insight into the magnitude of local strain about In ions in dilute InGaN—this may give rise to pronounced local piezoelectric effects, given that the piezoelectric coefficients in III-N materials are very large in magnitude [51].

We also note that the widths of the peaks decrease as the InN content is decreased from $x = 0.5$. This implies, for example, that for $x = 0.1$, 50% of the bonds in the peak near the GaN bond length lie within 0.005 Å of the mean, whereas for the corresponding peak in the alloy with $x = 0.5$, only 25.4% of the bonds are within this distance from the mean. This indicates a lower frequency of highly strained local environments about Ga ions at lower InN content, which stems from the fact that for lower InN content most Ga ions mainly have Ga ions as their second nearest neighbors. A similar analysis holds for the peak width near the unstrained InN bond length. We will discuss consequences of the local strain on the piezoelectric properties in more detail below for a QW wherein even larger strains feature.

We may gain further insight into the impact of local fluctuations in the strain by finding the local interatomic potential energy at each atomic site. To do this, we evaluate the "two-body-energy per atom:" at a given site in the relaxed structure, we sum the two-body interaction energies [given by Eq. (2)] of the ion with its four nearest neighbors and divide by 2 (in ZB, the bonds and ions are in 2-1 correspondence, i.e., there are "two bonds to every ion"). We elect to omit the three-body energy as its inclusion is more difficult and is expected to yield no new information. Figure 7 depicts the distribution of "atomic two-body energies" for the same two compositions as in Fig. 6, namely, 10% and 50% InN content in InGaN. Five peaks can be seen in the figure—one to each of the possible nearest-neighbor configurations (N surrounded by four Ga; by three Ga and one In, etc.). Of course, Ga surrounded by four N is equivalent to N surrounded by four Ga, so such a case is included in the leftmost peak; the analog for In. The two-body energies of the unperturbed configurations are indicated by dashed vertical lines (the ideal, unperturbed energy is computed from ideal bond lengths). It can be seen that each peak is shifted above its ideal energy by local strain. Furthermore, we observe that reducing the InN content lowers the energies of the "majority Ga sites" (i.e., the two leftmost red peaks), while raising those of the "majority In sites" and reducing the peak widths. This is in accordance with what was found earlier, giving rise in the case of 10% InN to the picture of a mostly strain-free GaN matrix embedded with In sites featuring high strain energies.
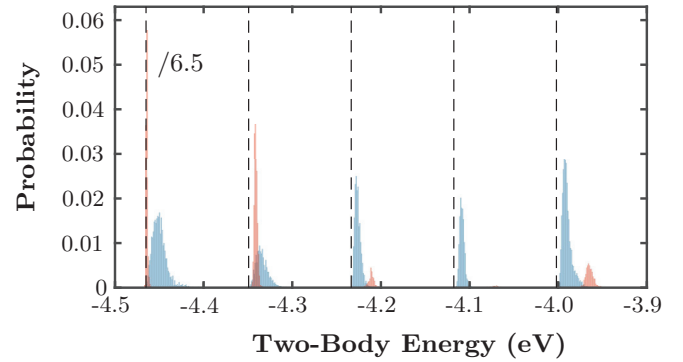

FIG. 7. The two-body energy per ion in the case of 50% (blue) and 10% (red) InN. The vertical lines mark the ideal energy for each nearest-neighbor configuration. Note that the leftmost red peak is actually 6.5 times larger than displayed here.

One might like to mimic the structural properties of InGaN when grown epitaxially on ZB GaN whereby the InGaN is strained to have the same lattice spacing as the GaN substrate along the x and y directions [(001) plane]. This scenario may be approximated in simulation by constraining the in-plane supercell lattice vectors to have length $11 \times a_0^{GaN}$ throughout relaxation and force all three lattice vectors to remain orthogonal. The cell is free to relax along the z direction, and all ions [save that at (0,0,0)] are allowed to relax internally. The resulting distributions are displayed in Fig. 8 (both distributions correspond to the same 50% InN random configuration from Fig. 6). The interpretation of these graphs is analogous to above. Note that, aside from the different areas bounded by the peaks, the effect of straining to the substrate is similar to that of lowering the InN content, in that the peak positions undergo similar changes. In particular, the average local strains associated to the GaN and InN peaks in the strained distribution are 0.092% and -2.186%, respectively. It is interesting that straining to the substrate forces the GaN peak to be almost symmetric about b_0^{GaN} so that about half of the Ga-N bonds are compressively strained.

Having discussed the impact of the alloy fluctuations on local strain effects, we aim now to study the consequences of these perturbations for local electrostatic built-in fields. The results of this analysis are presented in the following section.

C. InGaN/GaN quantum well

We next study the effects of random alloy fluctuations inside an InGaN QW on local strain, and finally the local piezoelectric potential, using the method outlined in Sec. II B and the Appendix. The supercell measures 7 unit cells along the two in-plane directions and 27 along the [001] direction, which is the growth direction of the QW. The cell contains 10 584 ions. After relaxation, the supercell measures $\approx 3.14 \times 3.14 \times 12.2$ nm^3. Here again, in order to simulate straining to a GaN substrate, the in-plane lattice vectors are constrained to the corresponding GaN lengths, and the lattice vectors are kept orthogonal. The QW width is approximately 2.32 nm. Since we seek first insights into how *local* alloy and strain fluctuations impact the *local* piezoelectric potential, the system size chosen should be sufficient for our purposes. The
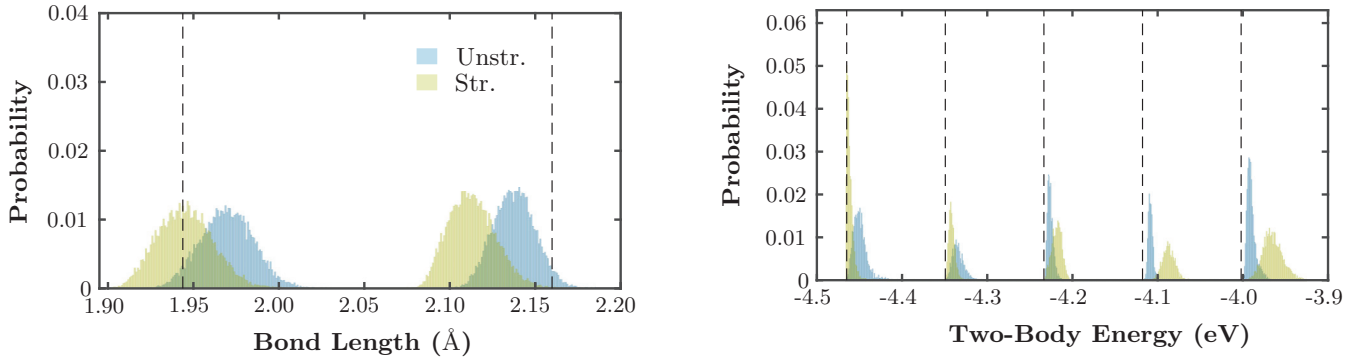
FIG. 8. The bond length and two-body energy distributions with and without straining to the substrate (both with 50% InN). The blue peaks are, thus, the same in this figure as in Figs. 6 and 7. The vertical lines are described in the main text and Fig. 7.

QW InN content is 15%, which is an experimentally viable [29] InN content; the remainder of the supercell is pure GaN. As before, the random In ion distribution is achieved using a random number generator.

We first extract strain profiles of the relaxed QW. Figure 9 shows the on-diagonal components of the strain tensor ϵ_{ii} as functions of the z coordinate along the growth direction ([001] direction). In Fig. 9(a), an average is taken over each horizontal ionic plane. After relaxation, most ions will have migrated from their initial planes—however, this migration is very small, so ions which start in the same plane finish on approximately the plane which is at the average of their final z coordinates. In continuum-elasticity theory the strain tensor components ϵ_{xx}, ϵ_{yy}, and ϵ_{zz} for growth along the [001] direction/z axis are given by [84]

$$\epsilon_{xx} = \epsilon_{yy} \quad \text{and} \quad \epsilon_{zz} = -\frac{2C_{12}}{C_{11}}\epsilon_{xx}, \quad (12)$$

which is on average consistent with our data. Using the bowing parameters given in Sec. III B for the elastic constants of bulk InGaN, the ratio $2C_{12}/C_{11}$ can be estimated at 15% InN as ~1.11. Assuming this value, Fig. 9(a) approximately obeys Eq. (12): (i) The compressive in-plane strains are approximately equal, and (ii) ϵ_{zz} is slightly larger than $-\epsilon_{xx}$. However, although the relations between the average strain components in Fig. 9(a) are predicted by Eq. (12), a continuum approach cannot give any information about the *local* profiles of these

components. As Fig. 9(a) shows, the different average strain tensor components undergo rapid random fluctuations inside the QW. Figure 9(b) depicts the strain along a single line scan (i.e., with x and y constants). A standard continuum method will not reproduce such a profile since it neglects alloy fluctuations; there is no obvious simple relation among the three components. Note also the magnitudes of the *local* strain fluctuations with (for example) ϵ_{yy} undergoing a change of ~3% over about 5 Å at one point. At a number of locations in the well (not depicted), we record *local* strains of $\gtrsim 8\%$. These strains can give rise to very large local electrostatic fields as we will see below.

Figure 10 shows a contour plot of the built-in piezoelectric potential in one x-z plane in the QW. All calculations have been performed employing a static permittivity $\varepsilon^D = 9.86\varepsilon_0^D$ throughout the supercell, where ε_0^D is the vacuum permittivity using a linear interpolation between InN and GaN values given in Ref. [85]. The plane (for which $y \approx 17\,\text{Å}$) contains only cations, but contour plots for other planes (anionic and cationic) are qualitatively similar. The most salient feature of the plot is the magnitude of local fluctuations of the piezoelectric potential ϕ. In a continuum picture, there would be no built-in potential at all, given that shear strains in the case of a QW grown along the [001] direction are zero. Our atomistic results are, thus, in stark contrast with such a picture, revealing a rapidly varying potential landscape. These potential variations give rise to strong electric fields—for example,
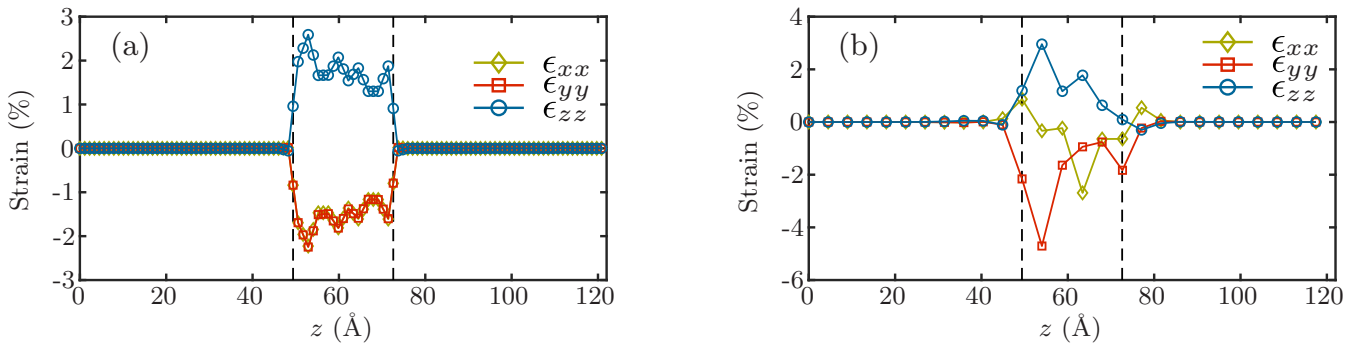

FIG. 9. (a) depicts the on-diagonal strain components ϵ_{ii}, averaged over horizontal atomic planes as functions of the z coordinate along the [001] direction, whereas (b) shows the components along a single line through the QW. The dashed lines indicate the approximate locations of the interfaces of the well.
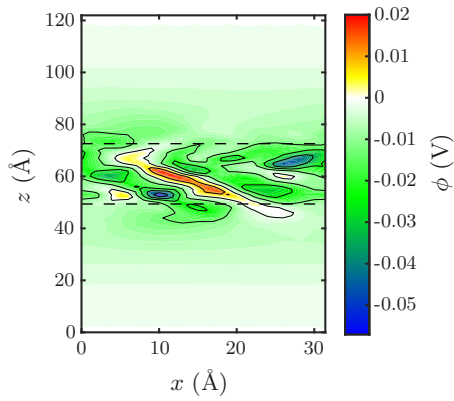
FIG. 10. Contour plot of the built-in piezoelectric potential on a single x-z plane in an $In_{0.15}Ga_{0.85}N/GaN$ QW. The dashed lines indicate the approximate locations of the well's interfaces.

at $(x, z) = (12, 55)$ Å, the field is about 3×10^8 V m^{-1} in norm. Furthermore, the potential energy in the nearby deep minimum at $(x, z) = (10, 53)$ Å for a carrier with charge $\pm e$ is 61 meV in magnitude, which gives an indication of the expected deformation of the conduction-/valence-band edge near this point (which is an In site). Potential energies of magnitudes up to 160 meV are recorded at other points in the well. Finally, note that there is a nonzero potential in the GaN buffer layers near where they meet the active layer.

We next briefly discuss consequences of these potential fluctuations for the electronic properties of the well. Ideally a full electronic structure calculation should be performed to gain detailed insight into this question. However, this is beyond the scope of the present paper, which aims rather to establish an atomistic SW-based description of local strain and piezoelectric potential, which is a prerequisite for atomistic electronic structure calculations. We may, however, glean some insight by considering the results of previous works. From Ref. [86], the effective masses of the heavy-hole (hh) band in the [100] and [110] directions in ZB $In_{0.15}Ga_{0.85}N$ are (assuming a linear dependence on InN content) $m_{hh}^{[100]} = 0.814m_0$ and $m_{hh}^{[110]} = 1.382m_0$, where m_0 is the free-electron mass. These two directions lie on the growth plane of our QW. The out-of-plane (along the [001] direction) mass is $m_{hh}^{[001]} = 0.814m_0$. On the other hand, in WZ $In_{0.15}Ga_{0.85}N$, the c-plane effective mass of the A band is $m_A^\perp = 0.299m_0$ and the mass along the growth direction is $m_A^\parallel = 1.866m_0$. As we can see, the effective masses are very comparable in magnitude. In general, the larger the effective mass of a carrier, the more susceptible is the carrier to these potential fluctuations, which, in turn, may lead to carrier localization effects (see, for instance, Refs. [40,75]). This argument is further supported by calculations in the literature on bulk ZB InGaN systems, which find hole localization effects even though these studies neglect local polarization field fluctuations [87]. Furthermore, in Ref. [41], the authors observe fluctuations of the built-in potential in a c-plane $In_{0.15}Ga_{0.85}N/GaN$ QW that are on the same order of magnitude as those seen here. That work considers wells with and without well-width fluctuations, but in all cases reports strong in-plane localization of holes, which is attributed to random-alloy effects. Hence, we may expect that

the in-plane hole effective masses in the system considered here are sufficient to cause them to localize in the presence of the fluctuations observed. By analogy to WZ-based systems, we conclude that such localization should have a strong effect on radiative recombination rates in devices utilizing ZB InGaN/GaN QWs.

Turning to electrons, it has been observed in the literature that the ground-state charge densities are significantly perturbed by random potential fluctuations [41] in c-plane InGaN QWs. Furthermore, the electron effective masses in ZB and WZ are almost equal [86]: $m_e^{ZB} = 0.172m_0$ and $m_e^{WZ} = 0.181m_0$ (where we have used an isotropic approximation for WZ since $m_e^{WZ,\perp}$ and $m_e^{WZ,\parallel}$ are very similar). Electrons are, therefore, likely to respond similarly in both systems to local potential variations (this has also been reflected by previous literature results on bulk ZB InGaN systems [87]). In general, then, we can expect that the optoelectronic properties of ZB InGaN/GaN QWs are strongly affected by local alloy fluctuations and that these effects (which have not in the past been considered in such wells) must be taken into account in order to model and understand these systems correctly so that the ZB III-nitrides may be exploited in novel devices to the fullest extent possible.

IV. CONCLUSION

In conclusion, we have presented an atomistic theoretical study of local strain and piezoelectric potential effects in bulk zinc-blende InGaN and an InGaN/GaN QW using a Stillinger-Weber potential. The here-developed local polarization model is general and can be used in conjunction with any semiempirical model that targets strain effects on an atomistic level. Building on this framework, we have demonstrated that local alloy fluctuations and the connected fluctuations in the strain field can lead to significant *local* strain-dependent piezoelectric potentials in zinc-blende InGaN/GaN QWs. Continuum-based models previously used in the literature overlook these effects, but our results give strong evidence that they should have a large impact on the electronic structure and ultimately the performance of devices utilizing such wells.

Additionally, we have shown that our developed Stillinger-Weber potential predicts using our here-established parameter sets, Kleinman parameter values for the zinc-blende III-nitrides that are in very good agreement with hybrid functional DFT literature data; the value for InN agrees almost perfectly with *ab initio* data (deviation $= -1.5\%$), and that for GaN is in reasonably good agreement ($+12.8\%$). Moreover, we find an almost perfect linear variation of the lattice constant of $In_xGa_{1-x}N$ alloys with InN content x over the full composition range, in agreement with literature experimental [33] and DFT [47,82] data. This also acts as compelling evidence that the developed Stillinger-Weber model reproduces ternary material parameters, without being fitted to these quantities. Following on from this, we predict bowing parameters of $b_{11} = 35.64$ GPa and $b_{12} = 0.68$ GPa for the x dependence of the elastic constants C_{11} and C_{12}, respectively. This information may now serve as input for continuum-based models, which require information about the composition dependence of involved material parameters. Furthermore, our analysis of bond

lengths and two-body energies per ion in bulk (freestanding) InGaN gives insight into the magnitude of local strain fields in this alloy; in particular, we find that in low-InN-content InGaN ($\sim$10%), the GaN-rich areas are almost strain-free on average, whereas In sites suffer large local strains of $\sim$2%.

Finally, our analysis of a ZB $In_{0.15}Ga_{0.85}N$/GaN QW demonstrates the magnitude and importance of the local strain field and associated piezoelectric potential in such systems. Local strain values of $\gtrsim$8% are observed at a number of lattice sites, and, in general, the strain field varies very rapidly over the scale of a few angstroms and cannot be accounted for using standard continuum models. The strain-induced piezoelectric potential also fluctuates strongly on small length scales, giving rise to local electric fields of up to $\sim10^8$ V m^{-1}, and potential-energy minima/maxima of depth/height $\sim$100 meV are observed at a number of points. By comparing the magnitudes of the potential fluctuations with those seen in wurtzite polar QWs [41] with the same InN content wherein hole localization and random alloy effects play key roles as well as considering the carrier effective masses, we conclude that these hitherto uninvestigated effects have a considerable impact on the optoelectronic properties of zinc-blende InGaN/GaN quantum wells. Overall, our results support (strong) carrier localization effects in ZB InGaN alloys and quantum wells, which will be investigated in further detail in future studies.

ACKNOWLEDGMENT

APPENDIX: MODIFIED FINITE-DIFFERENCE SOLUTION TO POISSON'S EQUATION

We use the method of finite differences to approximate derivatives numerically in this paper. However, whereas in "conventional" finite-difference problems the function of interest is known/to be found on a regular grid, we deal here with a ZB grid that has undergone relaxation due to random composition fluctuations, and so the method must be modified. Consider a function $f(\mathbf{r})$ defined on the grid. Starting at a fixed grid point $\mathbf{r}_0$, which may be a cation or nitrogen site, we suppose that its four nearest neighbors are at positions $\mathbf{r}_1, \ldots, \mathbf{r}_4$ *relative to* $\mathbf{r}_0$ in the ZB lattice. One may consider the derivative $\frac{\partial f}{\partial x}$ without loss of generality (the other two are

analogous). For the strain situations relevant for the present paper, it can be assumed that two of the relative nearest-neighbor positions (say $\mathbf{r}_1$ and $\mathbf{r}_3$) in the tetrahedron will have a positive x coordinate and the other two negative. We then average f at $\mathbf{r}_1$, $\mathbf{r}_3$ and at $\mathbf{r}_2$, $\mathbf{r}_4$, and form the symmetric difference quotient,

$$\frac{\partial f}{\partial x}(\mathbf{r}_0) = \frac{[f(\mathbf{r}_1) + f(\mathbf{r}_3)]/2 - [f(\mathbf{r}_2) + f(\mathbf{r}_4)]/2}{(x_1 + x_3)/2 - (x_2 + x_4)/2}. \quad (A1)$$

Note, the equality is only approximate, but the equality sign is used for typographical simplicity. The expression for the divergence term in Eq. (6) follows immediately. Equation (7), however, involves second derivatives, so we must apply Eq. (A1) twice. It will prove convenient to rewrite Eq. (A1), with $f = \phi$ as

$$\frac{\partial \phi}{\partial x}(\mathbf{r}_0) = \frac{\sum_{i=1}^{4} \text{sgn}(x_i - x_0)\phi(\mathbf{r}_i)}{\sum_{i=1}^{4} |x_i - x_0|}, \quad (A2)$$

where sgn is the signum function. Then, with $\partial_x \phi = \frac{\partial \phi}{\partial x}$, we have

$$\left[\frac{\partial}{\partial x}(\partial_x \phi)\right](\mathbf{r}_0) = \frac{\sum_{i=1}^{4} \text{sgn}(x_i - x_0)\partial_x \phi(\mathbf{r}_i)}{\sum_{i=1}^{4} |x_i - x_0|}. \quad (A3)$$

The derivatives $\partial_x \phi(\mathbf{r}_i)$ are then evaluated using Eq. (A2). After some algebra, we get

$$\nabla^2 \phi(\mathbf{r}_0) = \sum_{i,j=1}^{4} a_i^j \phi(\mathbf{r}_i^j) = -\frac{\rho(\mathbf{r}_0)}{\varepsilon^D}, \quad (A4)$$

where $\mathbf{r}_i^j$ is the jth nearest neighbor of $\mathbf{r}_i$ (so a second nearest neighbor of $\mathbf{r}_0$) and

$$a_i^j = \sum_{\xi=x,y,z} \frac{\text{sgn}(\xi_i - \xi_0)\text{sgn}(\xi_i^j - \xi_i)}{\left(\sum_{k=1}^{4} |\xi_k - \xi_0|\right)\left(\sum_{l=1}^{4} |\xi_i^l - \xi_i|\right)}. \quad (A5)$$

Here, the variable ξ runs over each of the Cartesian coordinates. There are n equations (A4)—one for each $\mathbf{r}_0$—giving rise to a matrix equation for the values of ϕ at the n ionic sites. The matrix is singular (corresponding to the nonuniqueness of the electrostatic potential) and sparse, so an appropriate solver must be used. If its rows are ordered so that the first $n/2$ correspond to cations and the rest correspond to nitrogen ions, then it is block diagonal so that each block may be considered separately.

[1] A. Zakutayev, J. Mater. Chem. A **4**, 6742 (2016).

[2] M. S. Wong, S. Nakamura, and S. P. DenBaars, ECS J. Solid State Sci. Technol. **9**, 015012 (2020).

[3] U. K. Mishra, L. Shen, T. E. Kazior, and Y.-F. Wu, Proc. IEEE **96**, 287 (2008).

[4] S. Nakamura and S. F. Chichibu, *Introduction to Nitride Semiconductor Blue Lasers and Light Emitting Diodes* (Taylor and Francis, London, 2000).

[5] S. Nakamura and G. Fasol, *The Blue Laser Diode* (Springer, Berlin, 1997).

[6] F. A. Ponce and D. P. Bour, Nature (London) **386**, 351 (1997).

[7] C. J. Humphreys, MRS Bull. **33**, 459 (2008).

[8] K. A. Bulashevich, A. V. Kulik, and S. Y. Karpov, Phys. Status Solidi A **212**, 914 (2015).

[9] D. Schiavon, M. Binder, M. Peter, B. Galler, P. Drechsel, and F. Scholz, Phys. Status Solidi B **250**, 283 (2013).

[10] M. Auf der Maur, A. Pecchia, G. Penazzi, W. Rodrigues, and A. Di Carlo, Phys. Rev. Lett. **116**, 027401 (2016).

[11] D. S. P. Tanner, P. Dawson, M. J. Kappers, R. A. Oliver, and S. Schulz, Phys. Rev. Appl. **13**, 044068 (2020).

[12] S. F. Chichibu, A. Uedono, T. Onuma, B. A. Haskell, A. Chakraborty, T. Koyama, P. T. Fini, S. Keller, S. P. DenBaars, J. S. Speck, U. K. Mishra, S. Nakamura, S. Yamaguchi, S. Kamiyama, H. Amano, I. Akasaki, J. Han, and T. Sota, Nat. Mater. **5**, 810 (2006).

[13] S. Chichibu, T. Azuhata, T. Sota, and S. Nakamura, Appl. Phys. Lett. **69**, 4188 (1996).

[14] T. Takeuchi, S. Sota, M. Katsuragawa, M. Komori, H. Takeuchi, H. Amano, and I. Akasaki, Jpn. J. Appl. Phys. **36**, L382 (1997).

[15] S. F. Chichibu, A. C. Abare, M. P. Mack, M. S. Minsky, T. Deguchi, D. Cohen, P. Kozodoy, S. B. Fleischer, S. Keller, J. S. Speck, J. E. Bowers, E. Hu, U. K. Mishra, L. A. Coldren, S. P. DenBaars, K. Wada, T. Sota, and S. Nakamura, Mater. Sci. Eng. B **59**, 298 (1999).

[16] A. Hangleiter, J. S. Im, J. Off, and F. Scholz, Phys. Status Solidi B **216**, 427 (1999).

[17] T. Takeuchi, H. Amano, and I. Akasaki, Jpn. J. Appl. Phys. **39**, 413 (2000).

[18] Y. Enya, Y. Yoshizumi, T. Kyono, K. Akita, M. Ueno, M. Adachi, T. Sumitomo, S. Tokuyama, T. Ikegami, K. Katayama, and T. Nakamura, Appl. Phys. Express **2**, 082101 (2009).

[19] K. Okamoto, J. Kashiwagi, T. Tanaka, and M. Kubota, Appl. Phys. Lett. **94**, 071105 (2009).

[20] A. Strittmatter, J. E. Northrup, N. M. Johnson, M. V. Kisin, P. Spiberg, H. El-Ghoroury, A. Usikov, and A. Syrkin, Phys. Status Solidi B **248**, 561 (2011).

[21] Y. Zhao, Q. Yan, C.-Y. Huang, P. S. S.-C. Huang, S. Tanaka, C.-C. Pan, Y. Kawaguchi, K. Fujito, C. G. Van de Walle, J. S. Speck, S. P. DenBaars, S. Nakamura, and D. Feezell, Appl. Phys. Lett. **100**, 201108 (2012).

[22] K. Xing, Y. Gong, J. Bai, and T. Wang, Appl. Phys. Lett. **99**, 181907 (2011).

[23] P. Waltereit, O. Brandt, A. Trampert, H. T. Grahn, J. Menniger, M. Ramsteiner, M. Reiche, and K. H. Ploog, Nature (London) **406**, 865 (2000).

[24] S. Schulz, D. P. Tanner, E. P. O'Reilly, M. A. Caro, T. L. Martin, P. A. J. Bagot, M. P. Moody, F. Tang, J. T. Griffiths, F. Oehler, M. J. Kappers, R. A. Oliver, C. J. Humphreys, D. Sutherland, M. J. Davies, and P. Dawson, Phys. Rev. B **92**, 235419 (2015).

[25] M. Anikeeva, M. Albrecht, F. Mahler, J. W. Tomm, L. Lymperakis, C. Chee, R. Calarco, J. Neugebauer, and T. Schulz, Sci. Rep. **9**, 9047 (2019).

[26] D. S. P. Tanner and S. Schulz, Nanoscale **12**, 20258 (2020).

[27] S. A. Church, B. Ding, P. W. Mitchell, M. J. Kappers, M. Frentrup, G. Kusch, S. M. Fairclough, D. J. Wallis, R. A. Oliver, and D. J. Binks, Appl. Phys. Lett. **117**, 032103 (2020).

[28] P. Seoung-Hwan and L. Yong-Tak, Chin. Phys. Lett. **27**, 044208 (2010).

[29] S. Li, J. Schörmann, D. J. As, and K. Lischka, Appl. Phys. Lett. **90**, 071903 (2007).

[30] C. M. Duque, M. E. Mora-Ramos, and C. A. Duque, Nanoscale Res. Lett. **7**, 492 (2012).

[31] I. Vurgaftman and J. R. Meyer, J. Appl. Phys. **94**, 3675 (2003).

[32] J. Schörmann, D. J. As, K. Lischka, P. Schley, R. Goldhahn, S. F. Li, W. Löffler, M. Hetterich, and H. Kalt, Appl. Phys. Lett. **89**, 261903 (2006).

[33] V. D. Compeán García, I. E. Orozco Hinostroza, A. Escobosa Echavarría, E. López Luna, A. G. Rodríguez, and M. A. Vidal, J. Cryst. Growth **418**, 120 (2015).

[34] J. F. Nye, *Physical Properties of Crystals: Their Representation by Tensors and Matrices* (Oxford University Press, New York, 1985).

[35] G. Bester, X. Wu, D. Vanderbilt, and A. Zunger, Phys. Rev. Lett. **96**, 187602 (2006).

[36] A. Beya-Wakata, P.-Y. Prodhomme, and G. Bester, Phys. Rev. B **84**, 195207 (2011).

[37] C. M. Jones, C.-H. Teng, Q. Yan, P.-C. Ku, and E. Kioupakis, Appl. Phys. Lett. **111**, 113501 (2017).

[38] D. S. P. Tanner, M. A. Caro, E. P. O'Reilly, and S. Schulz, RSC Adv. **6**, 64513 (2016).

[39] S. Schulz, M. A. Caro, C. Coughlan, and E. P. O'Reilly, Phys. Rev. B **91**, 035439 (2015).

[40] D. Watson-Parris, M. J. Godfrey, P. Dawson, R. A. Oliver, M. J. Galtrey, M. J. Kappers, and C. J. Humphreys, Phys. Rev. B **83**, 115321 (2011).

[41] D. S. P. Tanner, J. M. McMahon, and S. Schulz, Phys. Rev. Appl. **10**, 034027 (2018).

[42] S. Y. Karpov, Photonics Res. **5**, A7 (2017).

[43] X. Wu, E. J. Walter, A. M. Rappe, R. Car, and A. Selloni, Phys. Rev. B **80**, 115201 (2009).

[44] J. A. Chan, J. Z. Liu, and A. Zunger, Phys. Rev. B **82**, 045112 (2010).

[45] B. Lee and L.-W. Wang, J. Appl. Phys. **100**, 093717 (2006).

[46] P. G. Moses and C. G. Van de Walle, Appl. Phys. Lett. **96**, 021908 (2010).

[47] Y.-K. Kuo, B.-T. Liou, S.-H. Yen, and H.-Y. Chu, Opt. Commun. **237**, 363 (2004).

[48] C.-H. Kim and B.-H. Han, Solid State Commun. **106**, 127 (1998).

[49] D. A. Contreras-Solorio, J. Madrigal-Melchor, S. Jelev Vlaev, A. Enciso, and H. Hernández-Cocoletzi, Microelectron. J. **39**, 435 (2008).

[50] S. P. Łepkowski and I. Gorczyca, in *The Physics of Semiconductors: Proceedings of the 31st International Conference on the Physics of Semiconductors (ICPS) 2012*, edited by T. Ihn, C. Rössler, and A. Kozikov, AIP Conf. Proc. No. 1566 (AIP, New York, 2013), p. 83.

[51] M. A. Caro, S. Schulz, and E. P. O'Reilly, Phys. Rev. B **91**, 075203 (2015).

[52] S. Schulz, D. Mourad, and G. Czycholl, Phys. Rev. B **80**, 165405 (2009).

[53] P. M. Morse, Phys. Rev. **34**, 57 (1929).

[54] P. N. Keating, Phys. Rev. **145**, 637 (1966).

[55] R. M. Martin, Phys. Rev. B **1**, 4005 (1970).

[56] M. S. Daw and M. I. Baskes, Phys. Rev. B **29**, 6443 (1984).

[57] F. H. Stillinger and T. A. Weber, Phys. Rev. B **31**, 5262 (1985).

[58] M. Łopuszyński and J. A. Majewski, J. Appl. Phys. **111**, 033502 (2012).

[59] J. Tersoff, Phys. Rev. B **37**, 6991 (1988).

[60] J. D. Gale, J. Chem. Soc. Faraday Trans. **93**, 629 (1997).

[61] J. D. Gale and A. L. Rohl, Mol. Simul. **29**, 291 (2003).

[62] D. S. P. Tanner, A study of the elastic and electronic properties of III-nitride semiconductors, Ph.D. thesis, University College Cork, 2017.

[63] M. A. Caro, S. Schulz, and E. P. O'Reilly, Phys. Rev. B **86**, 014117 (2012).

[64] S. V. Novikov, N. Zainal, A. V. Akimov, C. R. Staddon, A. J. Kent, and C. T. Foxon, J. Vac. Sci. Technol. B **28**, C3B1 (2010).

[65] J. H. Edgar, *Properties of Group III Nitrides* (IEE, London, UK, 1994).

[66] H. Lei, X. J. Jiang, J. Chen, I. Belabbas, P. Ruterana, and G. Nouet, Phys. Status Solidi C **4**, 2449 (2007).

[67] H. P. Lei, J. Chen, S. Petit, P. Ruterana, X. Y. Jiang, and G. Nouet, Superlatt. Microstruct. **40**, 464 (2006).

[68] A. K. Kandalam, R. Pandey, M. A. Blanco, A. Costales, J. M. Recio, and J. M. Newsam, J. Phys. Chem. B **104**, 4361 (2000).

[69] S. K. Nayak, S. N. Khanna, and P. Jena, Phys. Rev. B **57**, 3787 (1998).

[70] J. L. Martins and A. Zunger, Phys. Rev. B **30**, 6217(R) (1984).

[71] K. Kim, W. R. L. Lambrecht, and B. Segall, Phys. Rev. B **53**, 16310 (1996).

[72] M. Zieliński, Phys. Rev. B **86**, 115424 (2012).

[73] M. Ichimura, Phys. Status Solidi A **153**, 431 (1996).

[74] Z. Q. Wang, D. Stroud, and A. J. Markworth, Phys. Rev. B **40**, 3129 (1989).

[75] M. A. Caro, S. Schulz, and E. P. O'Reilly, Phys. Rev. B **88**, 214103 (2013).

[76] G. Bester, A. Zunger, X. Wu, and D. Vanderbilt, Phys. Rev. B **74**, 081305(R) (2006).

[77] M. A. Migliorato, D. Powell, A. G. Cullis, T. Hammerschmidt, and G. P. Srivastava, Phys. Rev. B **74**, 245332 (2006).

[78] R. Garg, A. Hüe, V. Haxha, M. A. Migliorato, T. Hammerschmidt, and G. P. Srivastava, Appl. Phys. Lett. **95**, 041912 (2009).

[79] F. Raouafi, R. Benchamekh, M. O. Nestoklon, J.-M. Jancu, and P. Voisin, J. Phys.: Condens. Matter **28**, 045001 (2016).

[80] R. Benchamekh, S. Schulz, and E. P. O'Reilly, Phys. Rev. B **94**, 125308 (2016).

[81] L. Kleinman, Phys. Rev. **128**, 2614 (1962).

[82] Y.-C. Tsai and C. Bayram, Sci. Rep. **9**, 6583 (2019).

[83] M. Łopuszyński and J. A. Majewski, J. Phys.: Condens. Matter **22**, 205801 (2010).

[84] M. A. Caro, S. Schulz, S. B. Healy, and E. P. O'Reilly, J. Appl. Phys. **109**, 084110 (2011).

[85] P. Siddiqua and S. K. O'Leary, J. Mater. Sci.: Mater. Electron. **29**, 3511 (2018).

[86] P. Rinke, M. Winkelnkemper, A. Qteish, D. Bimberg, J. Neugebauer, and M. Scheffler, Phys. Rev. B **77**, 075202 (2008).

[87] P. R. C. Kent and A. Zunger, Appl. Phys. Lett. **79**, 1977 (2001).